COMET WIND

May 2023

Turbine Design Report

Prepared for the 2023 Collegiate Wind Competition Organizers and the U.S. Department of Energy

Mechanical Design Lead
Dan Bouzolin

Kinematics Lead
Kyle Mizumoto

Aero-structural Leads
Robin Reeves
Vinhson Ho

Foundation/Tower Lead
Colin Chaney

Electrical Design Lead
Fernando Harmjanz

Turbine-Side Electronics Lead
Jason Newman

Load-Side Electronics Lead
Pranav Marthi

Graduate Advisors
Thor Westergaard
A.S. Escalera Mendoza

Faculty Advisors
Dr. Todd Griffith
Dr. Matthew Gardner

UT DALLAS

COLLEGIATE WIND COMPETITION
U.S. DEPARTMENT OF ENERGY

Table of Contents

1. Executive Summary

The following report details the design, analysis, construction, and testing of a small-scale wind turbine by the UT Dallas Collegiate Wind Competition (CWC) team, otherwise known as Comet Wind. With this year's competition focus on offshore wind, our team has focused our efforts on designing a three-bladed, horizontal-axis, fixed-bottom offshore wind turbine with an active pitch and adjustable yaw system.

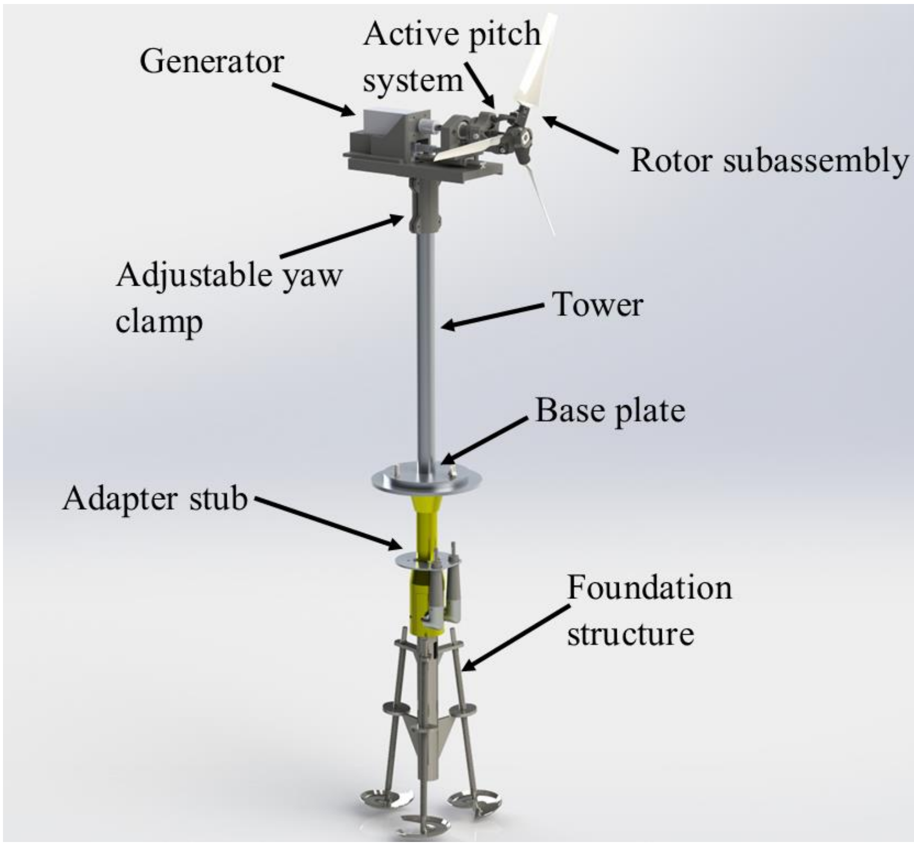

Figure 1: Final turbine design CAD model with constituent subassemblies shown

Our team is overseen by one Turbine Design Lead, who coordinates between the various mechanical and electrical aspects of the turbine. This student lead coordinates with the Mechanical Design and Electrical Design Leads, who further oversee subgroups at an even finer level. These subgroups are the smallest organizational structure within the team hierarchy before individual members, and consist of multiple members per group. On the mechanical side, these groups including the aero-structural team, kinematics team, foundation structure team. The electrical side is comprised of the load-side electronics team and turbine-side electronics team. An interdisciplinary subgroup – the pitch actuation team – consists of members from the kinematics team and turbine-side electronics team.

At a high level, the design includes several components ranging from structures designed to keep the turbine in place up to the actual power-producing components of the turbine. The mechanical design begins with the fully steel foundation structure, designed to interface with the sand-and-water competition tank via a screw-pile installation method. This foundation then connects to a competition-provided adapter stub, which clamps over the top of the foundation tubing and provides an interface for the turbine base flange and tower to attach to. Once the base and tower have been secured, the nacelle is fastened to the tower using a compressive clamp designed to allow for free yaw when loosened, but able to be securely tightened to prevent yaw during operation. The electrical design includes the turbine-side electronics involved in pitch actuation to reduce the aerodynamic forces on the rotor, as well as the load-side electronics used to vary current and ensure optimum power production.

Through our team's hard work, dedication, and innovation, we are proud to present our turbine for the 2023 Collegiate Wind Competition.

2. Design Objective

Our primary design focus was to balance the structural performance of our turbine with its power-producing performance, while still allowing for a great degree of control of rated power. To do so, our team fabricated a fixed-bottom foundation structure to secure the turbine in place, while simultaneously focusing on control methods such as active pitch control and buck-boost to maximize power production.

The team has worked tirelessly at developing new designs for our turbine prototype, making large improvements over last year's design. Last year, the team developed a fixed-pitch hub, did not manufacture a foundation structure, and had a simple load bank for electrical control. Though this year's design borrows a few aspects from last year's, namely the turbine base/tower assembly and the adjustable yaw compressive tower clamp, the majority of the design is completely new. The new design builds upon the building blocks of last year's design, but also implements an active blade pitching mechanism, more complex load-side and turbine-side electronics, and a steel foundation structure.

3. Mechanical Design

The mechanical design of our turbine primarily includes the foundation structure subassembly, but also extends to the structural and aerodynamic performance of our blades, as well as the structural performance of our tower, nacelle, and physical pitch actuation components.

3.1 - Blade Design, Analysis, and Testing

3.1.1 - Blade Design

The primary objective of our blade design process was to improve on the previous year's design, providing structurally sound blades that ensure safe operation of the turbine while maximizing our power production. Comet Wind's 2022 blade design was created with QBlade software using the NACA 6409 airfoil. The design had a maximum coefficient of power of 0.31 at a tip-speed-ratio of 3.5. During turbine testing at last year's competition, the blades demonstrated structural reliability with minimal tip deflection. The 2022 turbine produced approximately 18 Watts at 11 m/s, and survived wind speeds up to 15 m/s without the use of a pitching mechanism or brake system.

The goal for this year's design was to maintain the structural reliability attained with the previous year's design while improving the power production by increasing the rotor power and reducing the power losses through our direct drive system. To accomplish this, we planned to design blades with a higher coefficient of power than the previous year's design, which would operate at the highest efficiency rotational speeds of our generator.

The airfoils initially selected for the new designs were the AH7476, E71, E63-IL, and S1091 airfoils, chosen for their high lift-to-drag ratios at our expected Reynolds number of 50,000. We then used QBlade to create several single-airfoil blade designs from the selected airfoils, using the following Schmitz optimization formulas to determine the optimal chord and twist at each of the segments of our blades:

$$\phi = \frac{2}{3}\arctan\left(\frac{R}{r\lambda}\right) \qquad c = \frac{8\pi r}{BC_L}(1 - cos\phi) \qquad \theta_p = \phi - \alpha$$

where ϕ is the angle of the wind velocity relative to the rotor plane, R is the rotor radius, r is the radial distance to the segment, λ is the optimal tip-speed-ratio, c is the chord, B is the number of blades, C_L is the lift coefficient, θ_p is the angle of twist of the segment, and α is the optimal angle of attack of the airfoil. [1]

Our first designs were based on an optimal tip-speed-ratio of 5, corresponding with the optimal efficiency range of our generator (2000 - 2400 rpm) at wind speeds between 9 and 11 meters per second. The single-airfoil blade designs were then tested using QBlade simulations designed to mimic the competition testing tasks. Using the data from the simulations and generator performance data from the manufacturer, power curves were created for each blade, and their simulated Power Curve task scores were assessed. Next, a structural analysis was conducted of the two best performing designs, the S1091 and E71 designs, to determine the stress, bending moments, and deflection at each segment of our blades, using the aerodynamic loading from our QBlade simulations and the following equation to approximate the tip deflection:

$$\frac{M(x)}{EI} \approx \frac{d^2y}{dx^2}$$

where $M(x)$ is the bending moment, E is the modulus of elasticity, and I is the moment of inertia. [2]

Approximations of the cross-sectional areas and moments of inertia at each segment of the blade were calculated using the following formulas:

$$A \approx 0.6c^2\tau \qquad I \approx 0.036c^4\tau(\tau^2 + \varepsilon^2)$$

where c is the chord, τ is the thickness ratio, and ε is the camber ratio. [3]

The structural analysis indicated that both blade designs would experience significant tip deflection at the rated wind speed of 11 m/s unless manufactured from extremely stiff materials, such as composite resin or aluminum, with high modulus of elasticity. These materials are heavier, more expensive, and more difficult to manufacture than our other material options. Two solutions were explored: redesigning the current blades for a lower tip speed ratio to increase the cross-sectional area and creating new designs using airfoils with higher thickness-to-chord ratios.

Multiple iterations of the E71 and S1091 blade designs were created for lower optimal TSRs, which increased the cross-sectional area of the blades at each segment and reduced the tip deflection. However, this also reduced the maximum coefficient of power and lowered the operational rotor speed, reducing the efficiency of the generator during operation. Pursuing the second option, several airfoils with higher thickness-to-chord ratios were assessed and a new design was created using the FX-63 airfoil. This new design has a maximum coefficient of power of 0.349, an optimal TSR of 3.8 (Figure 2), and less expected tip deflection than any of our previous designs. Simulations of the rotor power and calculated generator power (Figure 3) indicate that the theoretical rated power will be approximately 35.6 W, nearly double the power production of last year's design. As such, it was selected as our official design choice for our 2023 blades.

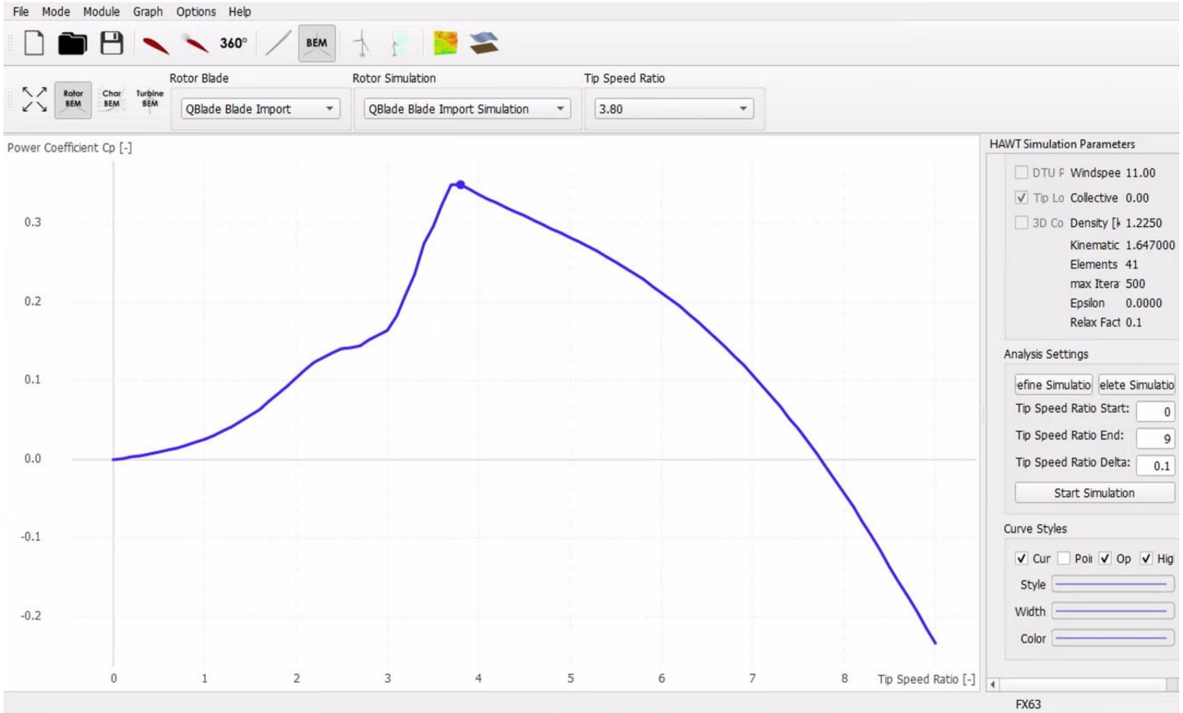

Figure 2: Cp-TSR curve of FX-63 blade design, generated using QBlade

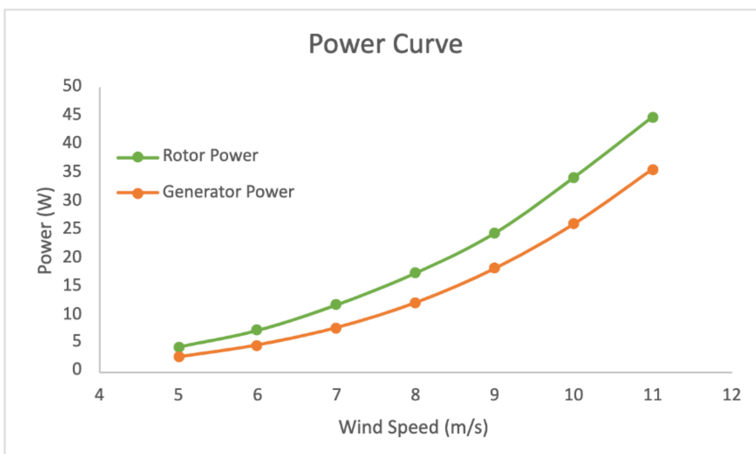

.

Figure 3: Simulated Power Curve of FX-63 blade design

An estimation of the annual energy production of the design was calculated using the theoretical rated power of 35.6 W, an assumed capacity factor of 0.50 for offshore turbines, and 12 hours of daily operation, giving the turbine an annual production of 78 kWh. [4][5]

3.1.2 - Blade Manufacturing

Blade materials were chosen based on cost, strength, and availability. From this, four materials were chosen: ABS, Carbon Fiber/Nylon composite, PLA, and EPIKOTE RIMR 135 epoxy resin [6]. In SolidWorks, each blade was analyzed as a static model with a distributed force applied to it to determine material strength and deflection (Figure 4). All blades were found to have a minimum factor of safety of at least 1, with PLA having the highest minimum factor of safety (at 1.986 under 10 N of force) for 3D printed blades. Structural analysis using SolidWorks finite element analysis reinforced the findings of our previous analysis, confirming that blades manufactured using resin would provide greater strength and resistance against tip deflection than PLA. However, the manufacturing process for resin blades is significantly more time consuming and difficult than printing methods like fused deposition modeling (FDM). It also requires a variety of different materials to be used in the process, such as casting tools and silicone to make a blade mold, and is considerably more expensive than FDM.

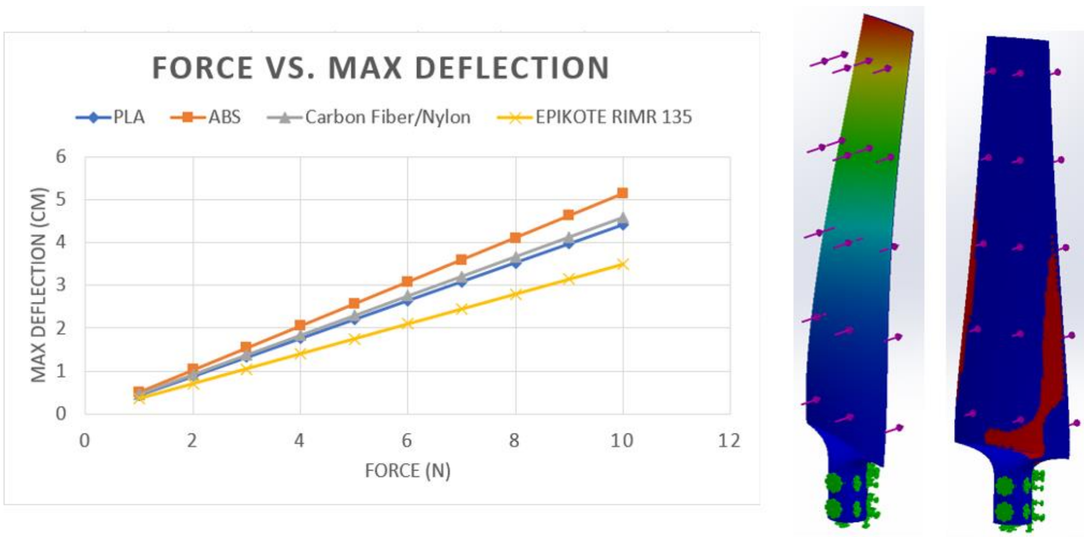

Figure 4: Analysis of E71 3.8 TSR blades using SolidWorks. Left: Graph of force vs. deflection. Middle: FEA of E71 to simulate deflection. Right: factor of safety analysis of PLA E71 blade.

Several of the original blade designs for this year were prototyped using our in-house printers, using ABS and PLA, as well as third party printers using Carbon Fiber/Nylon composite. Initial testing of the prototypes conducted in the outflow of our wind tunnel confirmed that stiffer materials were required to prevent tip deflection and ensure aerodynamic performance. Because the blades were so thin, 3D printing using traditional methods such as FDM proved to be difficult. Blades that were printed vertically maintained their original shape the best and printed with the highest resolution, but were structurally weaker compared to blades printed in other orientations. Blades lying horizontal would print with the worst geometric quality, showing stair-stepping and very unclean edges, but were the strongest. Blades printed with their leading edge on the print bed were of midrange quality between the other two orientations. Because printing the blades vertically most closely achieved the intended shape of the design, we chose to print our blades in this orientation. We found that the initial ABS, PLA, and Carbon Fiber/Nylon prototypes of our blades were fragile and deflected very easily. Structural analysis and SolidWorks FEA simulations illustrated that PLA was our strongest material option for 3D printing, followed by carbon fiber/nylon composite, then ABS, as shown in Figure 4. By increasing the cross-sectional area of our designs, we were able to print multiple viable blade designs out of PLA. Testing of our latest designs show improved tip deflection, as well as increased power production.

Research and experimentation was also put into fabrication of resin blades. A silicone mold using TinSil 80-15 [14] was initially used to create a mold by pouring it around a 3D printed blade. Once it was set, the blade was removed and a 3:1 mixture of EPIKOTE RIMR 135 epoxy and EPIKURE RIMH 136 was poured into the mold to create the blade. At this stage, the blade was very brittle and had to be demolded carefully to avoid fracturing. After demolding, the blade was put into an oven to cure and harden. Additionally, the process of creating each blade usually took several days to ensure proper setting of the resin. Ultimately, a fully resin blade was not able to be manufactured due to time constraints and the complicated nature of fabricating a resin blade. However, a lot was learned about the complex process of molding, such as resin properties and curing times, manufacturing effective molds, and successful demolding processes of the fragile blades before they get baked in the oven. Due to these reasons, 3D printing was selected as the optimal form of blade manufacturing.

3.2 - Pitch System Design, Analysis, and Testing

3.2.1 - Active Pitch Control Mechanism Design

Based on experiences with our turbine last year when we had a fixed-pitch design, as well as our observations of other teams at the competition, we knew early on that some kind of turbine control method would be necessary for our success in the competition. A large portion of our work early in the year was focused on researching and learning about the types of wind turbine control methods, from both sources online and from past team's Turbine Design Reports. As a result, we concluded that an active pitch control mechanism, in which the blade pitches are collectively altered by a linear force, was the best method for turbine control, as it could theoretically allow us to control turbine speed for the Control of Rated Power and Rotor Speed Task by pitching the blades to modulate torque and achieve desired power, and to facilitate turbine shutdown in the Safety Task by pitching the blades to full feather.

Designing the active pitch control mechanism proved to be a challenge. Although we were eventually able to perform valid analysis and testing (detailed later), early in the design process there were many unknowns. Most notably, we had very little reference for what the common failure points in an active pitch control mechanism are, and we also didn't know how extreme our loads might be, both in terms of the loads and stresses on each part due to high RPMs and in terms of the force required from the actuator to pitch the blades. Thus, some of the primary objectives in designing our pitch control mechanism early on were to reduce friction and reduce the intensity and complexity of the loads whenever possible. These were our objectives in addition to maximizing controllability, ensuring safety, and minimizing cost. Another influence in the design of the mechanism was our team's experience with and the cost and availability of PLA 3D printing, which allowed for cheap and relatively fast prototyping—a crucially important advantage for any team designing something new.

The final design of our active pitch control mechanism is shown in Figure 5. It is a combination of commercial parts and custom 3D-printed parts, and is actuated by a linear servo motor. The Mounts Hub holds the 3 Blade Mounts via heat-set insert threads, and connects to a shaft collar which is rotationally and axially fixed to the Splined Shaft. The Blade Mounts are secured to the heat-set inserts in the Mounts Hub via shoulder screws which allow for rotation. Each Blade Mount is also connected via shoulder screws to a Pitch Arm, all of which connect to the Arm Driver. Axial motion of the Pitch Driver causes Blade Mounts to collectively change blade pitch. The Arm Driver is mounted to the Linear Bearing which is rotationally fixed to the Splined Shaft, but which allows for low-friction movement along the shaft axis. We desired

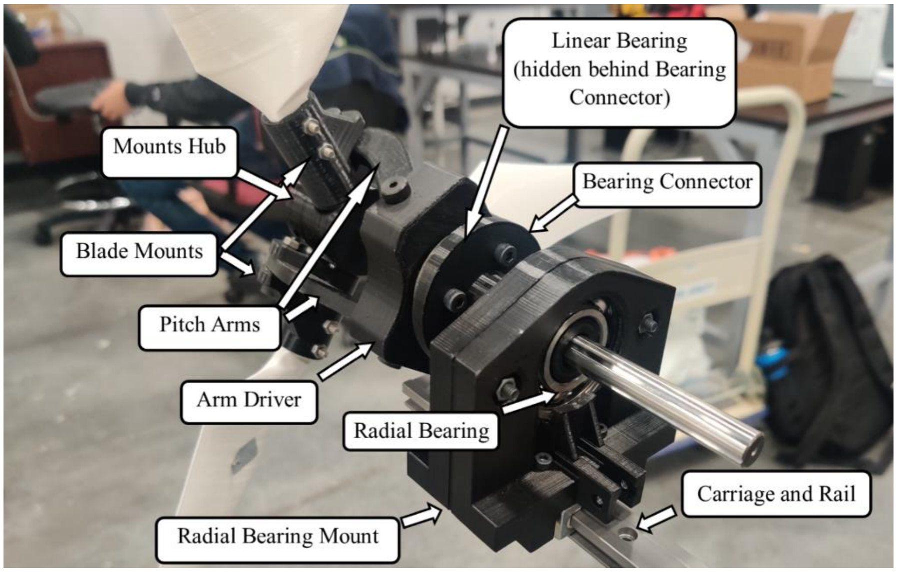

Figure 5: Final design of active pitch control mechanism

this type of interface in order to simplify the loads in the mechanism. Without a splined shaft, the rotation of the entire Linear Bearing Assembly would be driven not directly through the shaft, but indirectly, from the shaft to the Mounts Hub and eventually through the Pitch Arms, complicating and increasing the loads on these parts and potentially affecting pitch control performance. Mounted on the opposite face of the Linear Bearing flange, the Bearing Connector is press-fit into the inner ring of a radial bearing housed in the Radial Bearing Mount. The Radial Bearing Mount is designed to connect to the linear servo, and is also mounted onto a sleeve bearing Carriage and Rail. The Carriage and Rail serve to reduce friction acting against the forces from the linear servo, and to provide a stable point of support for the shaft through the Radial Bearing. The Radial Bearing Mount's axial position is coupled to the Linear Bearing Assembly, meaning that its movement causes changes in blade pitch.

One of the other ways in which we worked to minimize the force required from the actuator to pitch the blades was through a kinematic force analysis of the Blade Mounts and Pitch Arms using MATLAB. As shown in Figure 6, we will refer to the angle between the Blade Mount and the shaft as θ , which changes as the Blade Mounts rotate. The earliest concepts for our pitching mechanism were such that $\theta = 90°$ at full pitch and $\theta = 0°$ at full feather. However, we realized that at full feather, the Pitch Arms and Blade Mounts would form a straight line and would not be able to pitch back in at all. So, we modified the Blade Mounts to have an offset angle, ϕ , also shown in Figure 7, where at full pitch, $\theta = 90° + \phi$, and at full feather, $\theta = \phi$. Our goal with this analysis was to find the offset angle that would minimize the force needed to pitch the blades, realizing that that force varies as θ changes. Figure 6 shows the mechanism modeled as two connected linkages, where the Blade Mount is on a fixed pin, and the Pitch Arm is in a horizontal slot, which was used to derive equations relating the moment, M , to the force, F , required for static equilibrium. These were then utilized in a MATLAB script in which M was assumed to be constant and the lengths of the Blade Mount and Pitch Arm were inputted to obtain the graph shown in the right in Figure 6. It shows the minimum force, F , needed as θ changes from $10°$ to $170°$. The force is "relative" because the moment, M , used in the script does not reflect the actual pitching torque. Our mechanism would operate in some $90°$ range of that graph as it pitches to/from full pitch and full feather, depending on the offset angle used in the design. Therefore, the offset angle, ϕ , which minimizes the maximum force required over the $90°$ range of $\theta = \phi$ to $\theta = 90° + \phi$, is the optimal ϕ , $\phi_{optimal}$. $\phi_{optimal}$ was calculated to be $33°$. This MATLAB script also allowed us investigate the effects of changing the Blade Mount and Pitch Arm lengths, finding that the ratio between them is what affects the optimal angle. We were also able to use the MATLAB script to obtain the stroke length required for the optimal angle offset and inputted lengths, allowing us to choose the Actuonix L12-R Linear Actuator with 30 mm stroke length and 210:1 gear ratio.

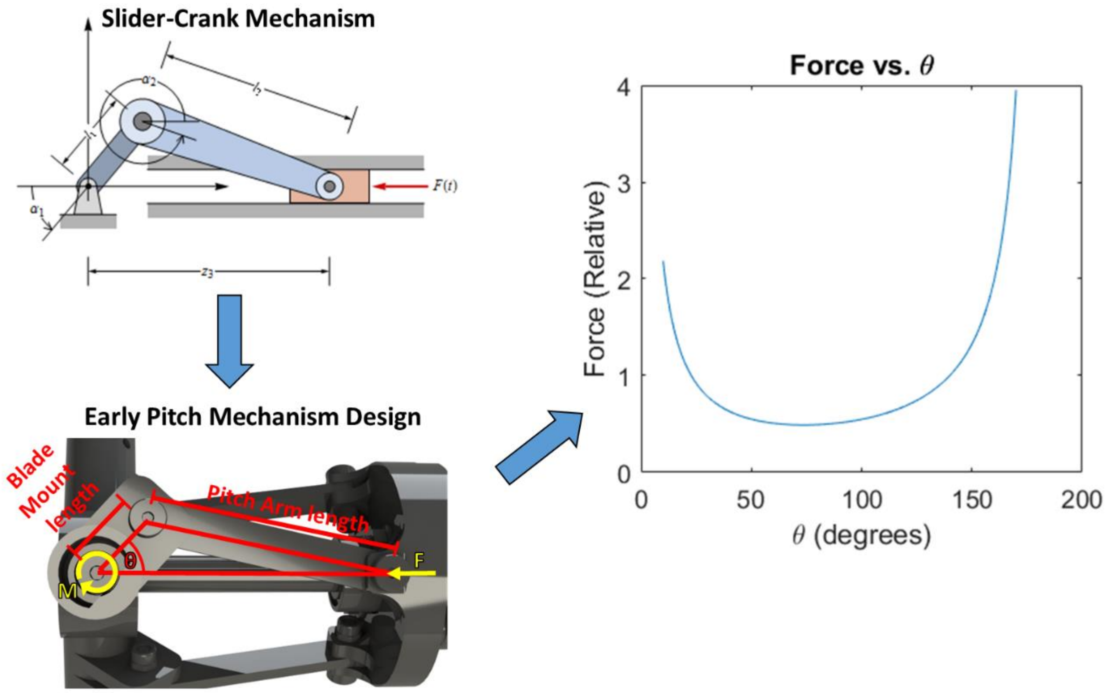

Figure 6: Blade pitch mechanism design evolution

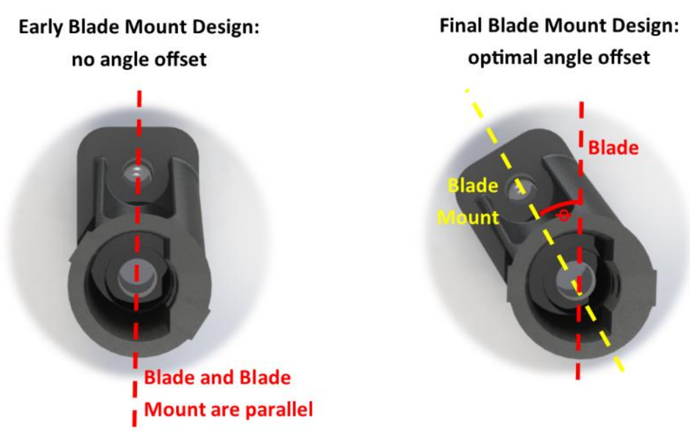

Figure 7: Blade Mount design evolution

3.2.2 - Strength Analysis and Testing

Because many key parts of the pitch mechanism are 3D printed, commonly accepted values for PLA's material properties, such as yield strength and Young's Modulus, may not reflect real world experience [9]. traditional FEA that the team is capable of may not produce results that accurately reflect the . Because of this, we often had to rely on testing rather than analysis, in order to ensure our parts could withstand the stresses of high wind speeds. Of the parts in the pitching mechanism, we first identified the most likely failure mode to be the heat-set inserts being pulled out of the Mounts Hub by the centripetal force from rotation at high RPM. Using CAD software to estimate the weight of a Blade Mount and blade, we found that at a worst-case scenario of 3000 RPM, which was determined by the airfoil and the electrical team, the centripetal force on the Mounts Hub shoulder screws and the heat-set inserts will be 296 Newtons. Although various tests available for viewing online show that heat-set inserts are capable of withstanding greater forces, the high variability of 3D printing settings and heat-set insert types motivated us to perform our own testing. The heat-set inserts that we are using for the Mounts Hub were shown in testing to be able to endure at least 600 N of pull-out force without experiencing any visible deformation or damage, giving us a factor of safety of at least 2.02.

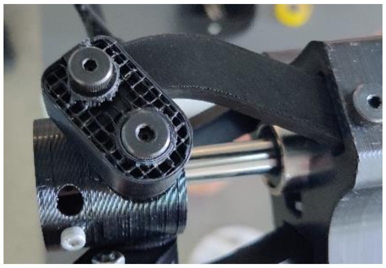

Figure 8: Blade Mount failure

During early testing of the entire turbine system at various wind speeds and at zero pitch, one of the Blade Mounts failed, as shown in Figure 8. The team is experimenting with various other 3D printing orientations [10], as well as increasing the perimeter count and infill, and will be continuing testing up to 3000 RPMs in order to find a safe design and print setting.

3.3 - Foundation Structure Design, Analysis, and Testing

The foundation structure for our wind turbine is essential for keeping the turbine assembly in place during operation. Because of this year's increased focus on offshore wind turbines, our team began looking to industry for the variety of offshore wind turbine foundations. Many offshore turbines in shallow water, similar to the testing tank in the CWC, use a gravity base, jacket structure, monopile, or tripod design to secure the turbine in place.

For this structure, it is imperative that the design can resist wind loading from the thrust forces acting on the turbine. Thus, this became our main design driver for the foundation structure. Our aero-structural team calculated the max thrust force of the turbine to be 11 Newtons of force, which can be used to calculated the approximate turning moment by multiplying the thrust by height from the rotor mid-plane to the top of our foundation structure as shown

$$11N \cdot .6m = 6.6\ N*m$$

In addition to the thrust force and overturning on the foundation, the team considered a number of other design requirements for the foundation structure, including weight, structural stability, each of fabrication, ease of installation, performance at small-scale, and compliance with the CWC rules. Based on the new no excavation and dimension constraints the team began brainstorming ideas on paper in a group giving inputs. The team favored the tripod design over the other 3 common types all considering design requirements being weight, rigidity, ease of fabrication, efficiency of installation, performance on a small scale and other compliances with CWC rules. A monopile design was decidedly would not resist lateral force well enough in the small scale, a jacket structure was unnecessarily complex, and a gravity base would be against the goal of creating a light weight design. Considering the trade-offs of each foundation type, the team selected the solid tripod with helical sand screws which use similar mechanics as an auger to anchor the foundation in place.

3.3.1 - Foundation Prototyping

The team began prototype production by drafting parts using SOLIDWORKS, then 3D printing them with a fused-deposition modeling process using PLA filament. Three models were printed and tested in a tote bin filled with play sand and water analogous to the competition tank. The first prototype was built with helical screws threaded into the feet and driven downward. In the first test, the plastic parts were difficult to install as the heads of the helical disk screws could not withstand the torque required to drive the structures in the sand and needed to be buried with excavation for testing purposes (Figure 11). In testing, the first structure stayed stable under 6.8 Nm of horizontal loading with two of the feet pointing in the opposite direction of the force but began to tip over with a 10.8 Nm force but began to tip after prolonged constant force causing the foundation to uproot. The forces of 6.8 and 10.8 Nm were chosen as stress test on the foundation to find if the structure could withstand the max thrust force and more for margin of error. This led us to design our second foundation which used thicker rods and larger disks with a lip lining the edges of the disk to increase anchoring force (Figure 10). This design would also have additional brackets for two points of contact on the rods and an angle outward 7.5 degrees to counterbalance the weight of the sand on the disk for additional rigidity (Figure 9). In testing the structure also withstood 6.8 and 10.8 N*m but then began to tip and the over stressed plastic pieces and helical disks snapped (Figure 12).

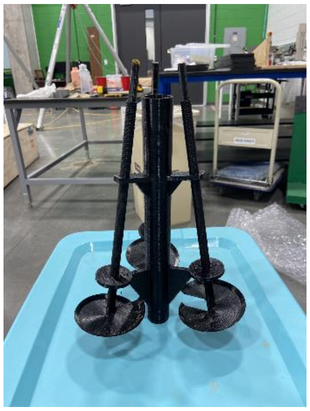

Figure 9: Plastic foundation prototype

Figure 10: 3D printed screw pile with lip

Figure 11: Foundation prototype installed into sand tank

From plastic prototype testing, the team learned about the stability of the design and was able to practice installation. The biggest takeaway was the installation practice the team learned with the second prototype which was done with two people. One team member would press the structure downward while the other would use a ratchet to drive the rod and helical disk combinations downwards into the sand. The one pushing down would alternatively check the levelness of the center pile to give feedback to the other ratcheting the rods. However, the PLA printed parts were not strong enough for proper data collection and only had minor improvements in design iterations, so a steel prototype would need to be fabricated for proper testing.

Figure 12: Foundation prototype failure

Figure 13: Foundation prototype testing

3.3.2 - Steel Foundation Manufacturing and Testing

The steel prototype will be most similar to the third PLA iteration but modified for steel fabrication and tested in the previously mentioned tote of sand. The design was fabricated from stainless steel in communication with the UT Dallas machine shop.(see figure)

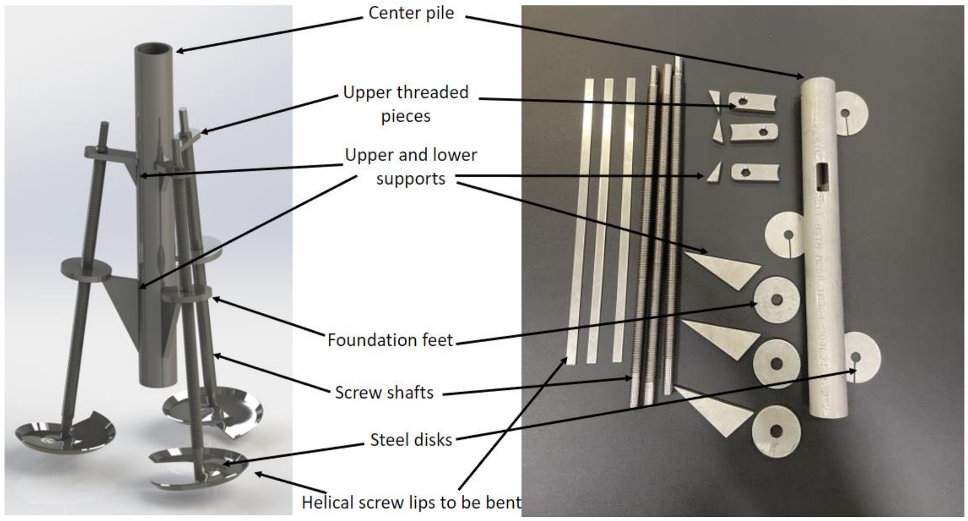

Figure 13: Steel foundation design (left) along with design manufacturing process (right)

In the new test there will be several different tests with differing independent variables which will measure the deflection of the center pile while experimenting with the foundation orientation, disruption of sand through vibration, and angle relative to the force. The foundation will be installed with 3 different orientations two of the feet pointing away from the applied force, one with one foot pointing away from force and another with the feet staggered. The second variable will be the vibration of the structure with an orbital sander to oscillate to disrupt pockets of less dense sand around the structure. The experiment will have two versions, one with vibration and the other without. Then the final independent variable would be the angle of the center pile relative to the force being 90 degrees where the top the foundation is perfectly level and the other where the top is angled a slight 7.5 degrees away from the force in a way predicting deflections so that the whole structure is level under thrust from moving air.

Each of these variables would be interchanged for different tests but they would still be subject to the same forces and the foundation tested for deflection. A string will be lined across the top of the tote touching the side of the center pile opposite the force. During the test, the deflection would be measured by the distance from the string.

4. Electrical Design

The electrical design of our wind turbine is split into two divisions of teams, the Turbine-Side Electronics and Load-Side Electronics. The Turbine-Side Electronics includes the generator choice, 3 phase rectification and filtering circuitry, as well as the design of the pitch controller through a linear actuator. The Load-side Electronics includes a DC-DC converter (in the form of a Buck Boost Converter) for current control, relevant driving circuitry, and a filter to reduce voltage ripple. Both Turbine-side and Load-side electronics include safety electronics to meet the safety tasks, sensors to measure power, RPM, and wind speed, as well as power distribution circuitry to ensure our sensors have power provided to them while complying to the competition rules. A diagram of both turbine and load side electronics can be seen in Figure 14.

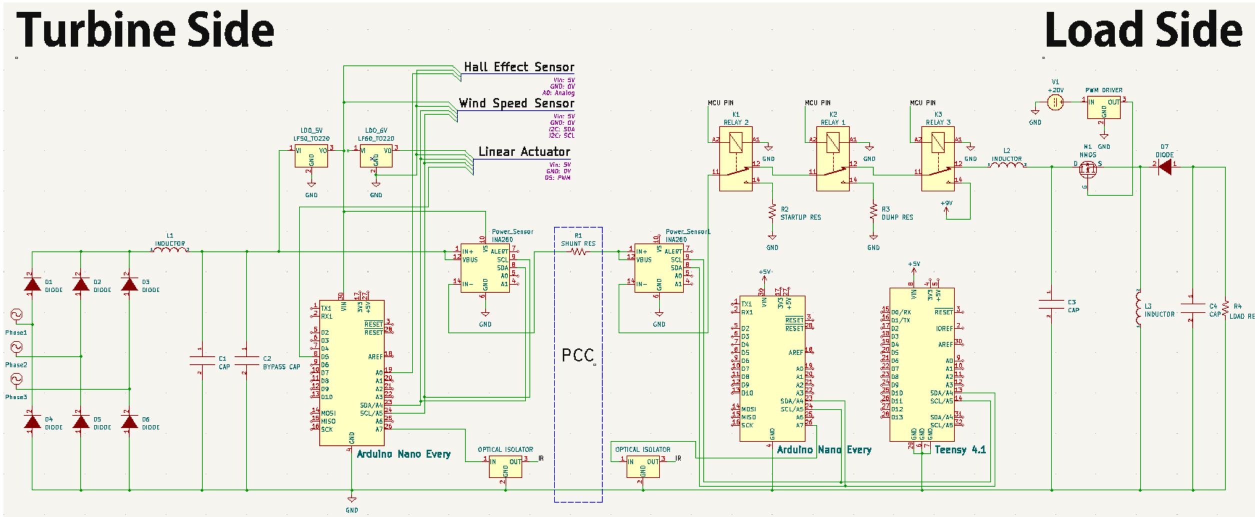

Figure 14: Final circuit schematic design of the turbine side and load side electronics designed in KiCAD

4.1 - Turbine-side Electronics

4.1.1 - Design Approach

Our team was inspired by the previous team's ability to enter into the Collegiate Wind Competition (CWC) 2022 for the first time as a learn-along team. Using both the knowledge gained from last year's competition as well as all the previous CWC contestants' design reports allowed us to gain a better understanding of how we should approach our own design. The design approach used throughout the competition timeline focused on building an understanding of the effect of each component within our design and its impact on turbine performance. In the following, sections we will elaborate on our thought process and further explain our decision-making process.

4.1.2 - Generator

As we were able to confirm during the participation as a learn along team at CWC 2022, our brushed DC generator design resulted in a large drop of efficiency due the mechanical rectification of the brushed contacts. To maximize efficiency, we are now using a brushless DC (BLDC) motor as our generator. Our first choice was the KDE3520XF-400 due to compatibility with the blade design of the time. After designing our current blades, calculations showed that the KDE3520XF-400 would not be the optimal generator for our system. Despite its high-power production, the voltage produced is low (as seen in Table 1), which has drawbacks due to the sensors placed in the turbine side electronics needing to be powered by the power we produce.

Windspeed (m/s)	Torque (Ncm)	RPM	Voltage	Current	Power (Watts)	Power Assuming 80% Elec. Eff. (Watts)	Score Weight	Points
5	5.5	800	2	2.301	4.603	3.682	0.7	2.577
6	7.4	1000	2.5	3.096	7.741	6.192	0.8	4.954
7	10.5	1200	3	4.393	13.180	10.544	0.8	8.435
8	13.4	1300	3.25	5.607	18.222	14.577	0.7	10.204
9	17.4	1500	3.75	7.280	27.301	21.841	0.4	8.736
10	21.1	1700	4.25	8.828	37.521	30.017	0.3	9.005
11	26	1900	4.75	10.879	51.674	41.339	0.1	4.134

***Table 1**: Windspeed and torque values for final blades and expected current, voltage, and power production using the KDE3520XF-400 BLDC generator and power curve scores*

The ElectroCraft RP17M32V24 is capable of producing high enough voltage and current to power our entire turbine side sensors as well as the actuator at very low windspeeds (shown in Table 2). This will allow us to use our sensors at lower windspeeds while maintaining similar power production compared to the KDE3520XF-400. Although we will not make use of the pitch actuator at this speed for RPM control under normal conditions, having full access to the RPM and windspeed measurements at low wind speeds will allow our system to have greater control of our turbines power production.

Windspeed (m/s)	Torque (Ncm)	RPM	Voltage	Current	Power (Watts)	Power assuming 80% Electrical Efficiency (Watts)	Score Weight	Points
5	5.5	800	7.36	0.625	4.600	3.680	0.7	2.576
6	7.4	1000	9.2	0.841	7.736	6.189	0.8	4.951
7	10.5	1200	11.04	1.193	13.173	10.538	0.8	8.431
8	13.4	1300	11.96	1.523	18.212	14.569	0.7	10.199
9	17.4	1500	13.8	1.977	27.286	21.829	0.4	8.732
10	21.1	1700	15.64	2.398	37.500	30.000	0.3	9.000
11	26	1900	17.48	2.955	51.645	41.316	0.1	4.132

***Table 2**: Windspeed and torque values for final blades and expected current, voltage, and power production using the RP17M32V24 BLDC generator and power curve scores*

4.1.3 - Rectification

Due to the significant impact of the rectification circuit on both the power ripple production and potential losses resulting from suboptimal parts, component research was a crucial step in our design. Schottky diodes are ideal for rectification due to their low voltage drop and fast switching speed. We procured multiple sets of Schottky diodes that matched our parameters and tested all of them. Lacking a reliable source of 3-phase AC generation, our team managed to construct a mounting configuration for a motor that was able to drive a BLDC motor as a generator to produce 3-phase AC. We were able to rapidly test the different sets of diodes we purchased and extract the necessary data to analyze our 3-phase rectification across our diodes. After extensive testing we selected our diodes, identifying the set that outperformed the other sets [7].

To address power loss concerns, an LC filter was added to attenuate unwanted frequencies. The following equation to determine the output frequencies of our LC filter:

$$f = 2 \cdot (Number\ of\ phases) \cdot (Rotational\ Speed\ in\ Hz)$$

The cutoff frequency of the LC filter was validated through in-house testing using inductors and capacitors of different values. Impedance calculations guided the selection of an optimal capacitance of 1mF and an inductance of 180uH. The designed LC filter was further validated through simulation using MATLAB/Simulink and practical testing with the BLDC generator as the 3-phase AC source.

Due to the low cost of electrolytic capacitors, we tested our design using several low-cost capacitors, after confirming the performance of our LC filter matched our simulated results, we updated our design to use a high-quality tantalum capacitor to reduce the losses associated with the high Equivalent Series Resistance (ESR) intrinsic to electrolytic capacitors. During wind tunnel testing, results indicated a 94.85% efficient LC filter, through the comparison of Volts/KRPM that was measured and that was supplied in the datasheet of the generator [8]. The average voltage production was measured at 3.75, 4.5, 5.5, and 6m/s at several pitch angles to achieve different rotational speeds and in turn voltage productions.

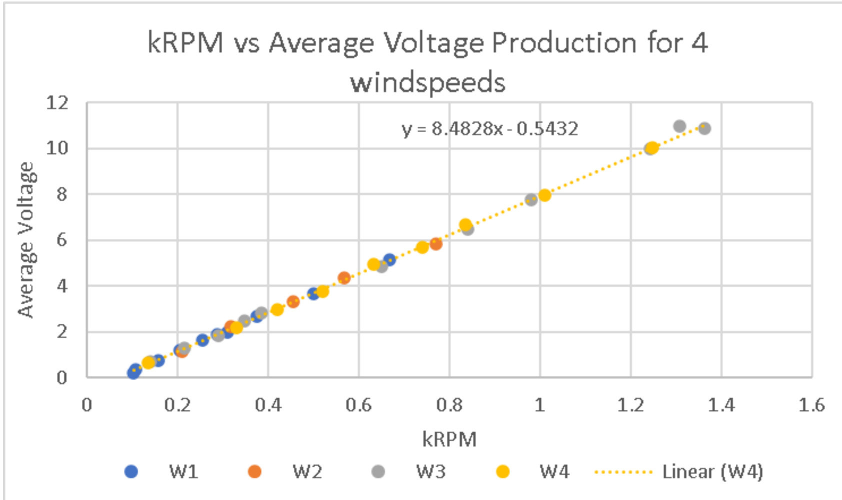

Figure 105: kRPM vs Voltage Production for 4 windspeeds and KV rating of Generator and LC filter system

During wind tunnel testing we experienced very low DC ripple, averaging around 10% or less across all output values even at low windspeeds (and corresponding frequencies). Our LC filter had a reduced ripple reduction functionality at lower rpm due to the intrinsic properties of LC filters (as shown in the wind tunnel testing results presented in Figure 16). Both the rectifier and LC filter were analyzed using an Analog Discovery 2 and Waveforms software.

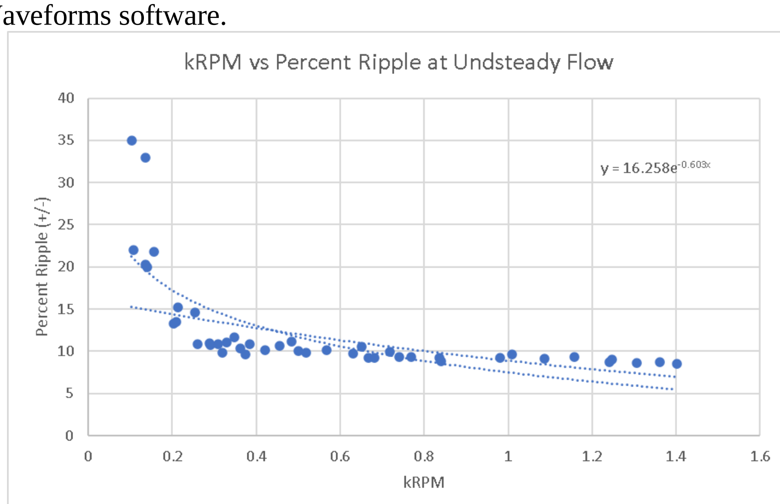

Figure 16: kRPM vs Percent Ripple at Unsteady Flow

4.1.4 - Voltage Regulation

Due to the importance of our sensors in the identification of the turbines operating regimes, we explored multiple options to provide power to the sensors and devices within the turbine side electronics, as outlined within the competition rules. Due to the added complexity of a DC-DC that uses active switching, a low-dropout regulator (LDO) was selected. The inefficiency inherent to LDOs is an acceptable drawback due to the low current requirements for our sensors. After initial testing of the LDO's an overlooked parameter was discovered, the ripple rejection or power supply rejection ratio (PSRR), which describes the capability of an LDO to reject (suppress) input voltage ripple. The formula for PSRR is described below:

$$PSRR \; = \; 20\log\left(\frac{Vinrpl}{Voutrpl}\right) \; dB$$

The new design includes a bypass capacitor to add in parallel with our rectified output which will reduce unwanted noise and assist with ripple rejection values of our more sensitive components.

4.1.5 - Safety

For the load disconnect condition, once current is zero, which will only occur at moment that load side will is disconnected from the turbine or during startup. Since during the load disconnect condition power will still be generated, a signal from the load side MCU to the turbine side MCU will result in the pitch actuator pitching to full feather to shut down the turbine as per competition rules. Within load side electronics the moment zero current is measured, power will be provided to the PCC until a response is received from the turbine side MCU indicating power has been received, afterwards power will be provided for 10 seconds, which gives the turbine side MCU sufficient time to pitch to zero degrees and allow restart. It is to be noted that the power provided by the load side electronics will only reach the turbine side electronics if the load is connected which only occurs during restart from the load disconnect condition and the startup of the turbine.

The emergency shut off task within turbine side electronics will follow the same procedure as the load disconnect condition, with the only difference being the trigger for the shutdown procedure coming from a normally closed emergency stop system. Within load side electronics the major difference in procedure from that of the load disconnect condition is that power will not be provided through the PCC until the emergency shutdown button has been deactivated. A full detailed flow chart is shown in Figure__ of both the turbine side and load side electronics system behavior throughout the turbine operation including the safety task, power curve, control of rated power and rotor speed task, and the durability task.

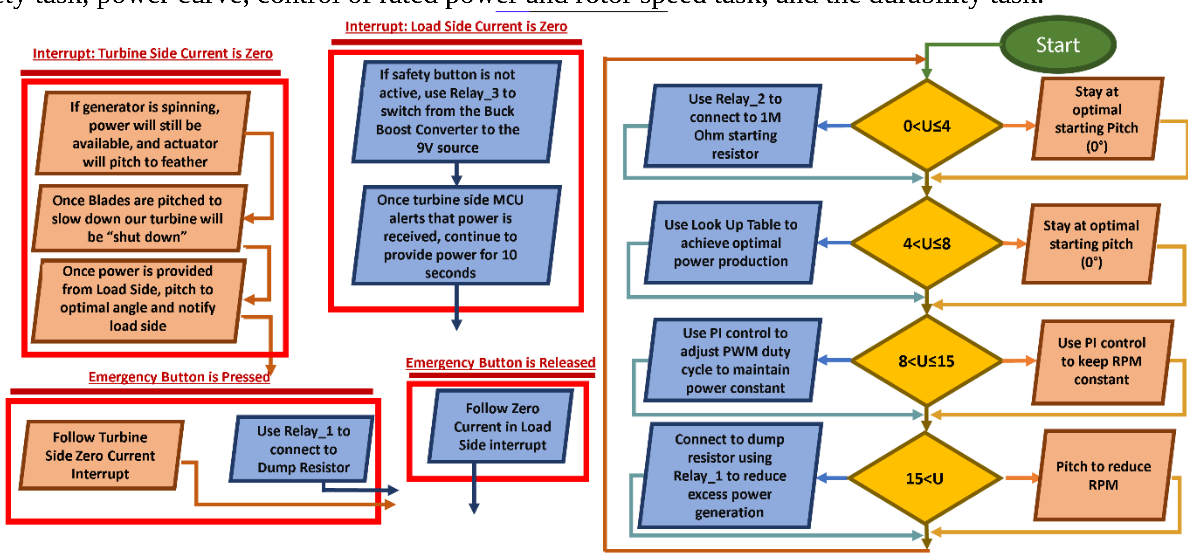

Figure 17: Turbine and Load side electronic system behavior throughout the different operating regions

4.1.6 - Pitch Control

One of the biggest challenges we have taken on as a team this year is to implement an active pitch control system. We have an assortment of sensors that use different serial communication methods whose primary purpose is to make pitch control achievable. These sensors include a linear actuator which operates our pitching mechanism, a hot wire anemometer used for measuring wind speed, a hall effect sensor that will measure RPM, and a power sensor for current, voltage, and power readings. All supporting code was created and tested using the Arduino IDE. Utilizing the object-oriented benefits of C++, individual objects were made for each sensor and their respective functions defined within the scope of their class.

The MATLAB System Identification Toolbox (SIT) allows us to plug in the raw data produced by the system to determine the transfer functions and calculate the necessary gain coefficients to utilize the ultimate sensitivity method also known as the Ziegler-Nichols method. Current testing methods yield a pitch to RPM relationship for various windspeeds (Figure 18), with the input being the millisecond input to the linear actuator and our output as the RPM. This gives us a transfer function that we then feed into the system control toolbox, which will give us a good estimate on the PI values required to reach the steady state value. These PI values will enable the pitch to adjust to whatever is best to reach our steady state value, which is 2000rpm. Pitch actuation will only occur between two parameters: 11-15 m/s and 15> m/s. This is due to the fact that the optimal pitch happens to be the same as the initial resting pitch at windspeeds below 11 m/s (opposite of full feather, idk what the technical term is pls help). From 11-15 m/s, pitch actuation begins to adjust to maintain 2000 rpm. Beyond 15 m/s, it adjusts to slow down rpm for safety reasons.

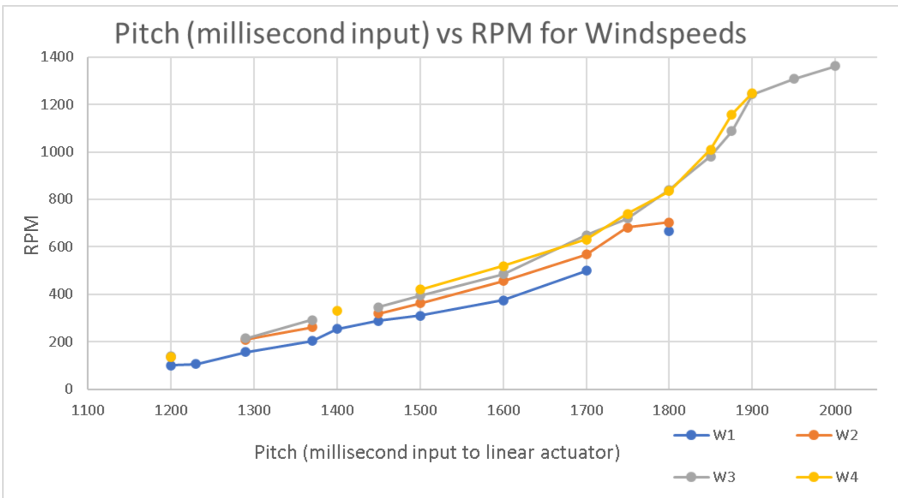

Figure 18: Pitch (millisecond input to linear actuator) vs RPM for 4 windspeeds

4.2 - Load-side Electronics

4.2.1 - Design Approach

The load-side electronics circuit regulates the turbine's power production by modulating the current flowing through the system. Our team's first decision was the type of system we would implement in conjunction with the Turbine-side Electronics team. As we examined last year's teams' Turbine Design Reports, most teams had implemented a load bank: a series of resistors placed in either a binary or parallel configuration that used power-controlled switches to vary the system's load and therefore achieve optimum power at different wind speeds. An alternative solution was the buck-boost converter. We considered this system a viable option as it is commonly used in full-sized turbines; the prospect of building a turbine model with similar components excited us. The difficulty of implementation lay in the complex nature of PWM signals controlling the circuit's effective impedance; furthermore, BBCs had fewer past implementations in this configuration with little documentation to refer to. As the voltage values are measured across the PCC, the "input" and "output" voltages are virtually the same (given that windspeed, RPM, and the blades' pitching angle do not change). We deduced that this meant that the MOSFET's duty cycle influenced the circuit's effective impedance. Overall, this power optimization method intrigued the team, and we decided to explore it as our solution for this year's competition.

4.2.2 - Buck Boost Converter Design

Our final circuit uses several key components to achieve optimal power production, including an LC filter, MOSFET, inductor, capacitor, diode, and load resistor. This system is controlled by a Teensy 4.1, our primary MCU, which also handles the safety tasks.

The MOSFET is a voltage-controlled transistor that switches between the on and off states of the BBC. Our nMOS transistor was explicitly chosen for its lower conduction losses, higher output voltage, and ability to handle faster switching speeds (100kHz). As the effective impedance of the circuit changes with the duty cycle, the current flowing through the BBC's inductor also changes, as illustrated in the formula below:

$$I_L = (V_S \cdot D)/(R(1-D)^2);\ V_S = Input\ voltage,\ D = duty\ cycle,\ R = load\ resistor$$

The MOSFET is connected to the high side of the BBC, requiring an isolated gate driver that controls the gate-to-source voltage. The gate-to-source voltage of the MOSFET must be greater than the voltage of the input source to turn the MOSFET on. Since this is equivalent to the input voltage (to the drain) plus the voltage drop across the MOSFET, the driver boosts the gate voltage. It also filters any PWM signal noise out, providing the nMOS with a clean and stable signal each cycle. The driver, with its minimal rise and fall times in nanoseconds and high noise immunity, is the perfect fit for amplifying and supplying the microcontrollers (Teensy 4.1) PWM signal to the MOSFET. These connections have been shown in Figure 19 below.

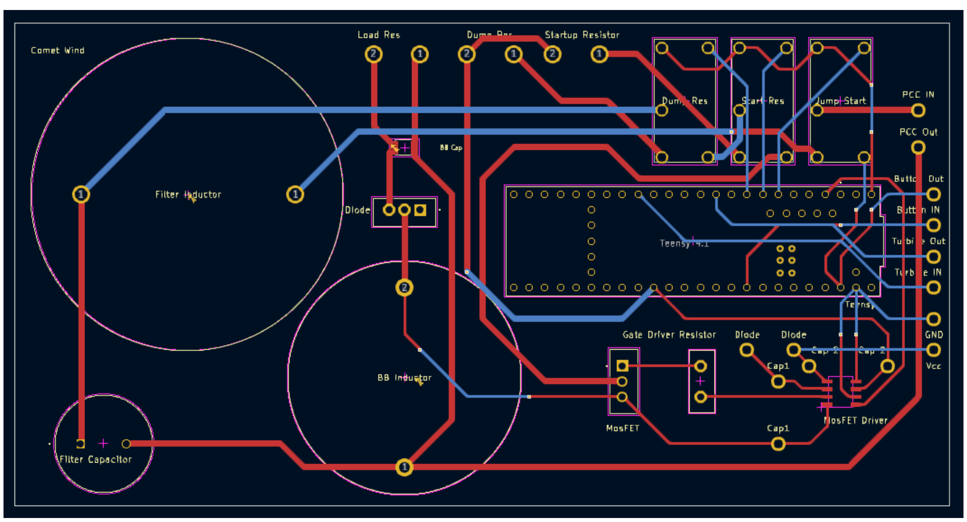

Figure 19: PCB Layout of Load Side Electronics

4.2.3 - Teensy 4.1 Microcontroller

An appropriate PWM frequency of 100kHz was chosen as it was higher than the inductor's resonant frequency while minimizing the output voltage ripple and switching losses [11]. Last year's winning team, Kansas State University, used a Teensy 4.1 to improve their system's data-tracking capabilities. Their success led us to explore Teensy's other advantages and determine whether it would perform better than other MCUs that fit our specifications. The Teensy 4.1 smoothly handles PWM operations at 100kHz, providing a high resolution of 16 bits, allowing for variation in duty cycle as low as 0.015% whichtranslates into modulating the inductor current on a scale of milliamps. The Teensy is I2C compatible and supports configurable clock speeds above the 100kHz PWM frequency used in the BBC. Its many analog and digital I/O pins and programmability using the Arduino IDE made the Teensy 4.1 our system's primary MCU [12]. The I2C protocol allows the MCU to collect this data from a power sensor, a Hall-effect sensor, and a windspeed sensor simultaneously, maintaining its quick response time. The Teensy and the IR2011 require external DC power supplies and will be powered through a 120VAC wall outlet provided to load side as noted in the competition rules [13].

4.2.4 - Testing, Coding, and PI Control

We programmed the MCU to identify the turbine's region of operation and power task triggers using specified wind speed. PI control is used for the normal operation region, with Look Up Tables (LUTs) for the startup region. The LUT was populated from the theoretical optimum current values, which have been converted to the corresponding PWM signal that the Teensy sends to the MOSFET. An example of a PWM signal being measured at the MOSFET's gate is shown in Figure 20. Our design utilizes three single pole double throw form C (SPDT) relays. The first relay will be used at windspeeds below 5m/s until startup and high power production is achieved, initially connecting the system to a 1MΩ resistor to reduce the electrical torque and allow the turbine to speed up. At windspeeds above 15m/s the second relay, a single pole double throw (SPDT) type controlled by the Teensy, will disconnect the circuit from the Buck Boost converter to a 30Ω dump resistor rated at 300W. The third relay, as well as the outline of the load and turbine side system behavior can be found under section 4.1.5.

Tuning the PI control on the Teensy proved to be difficult, with each term's stability, settling time, and overshoot having equal importance. Another problem we tackled was determining the exact scale factors used since they would need to be as accurate as possible to help the system reach the desired power production quickly. We settled on a scale and a range of integration factors for weighing each previous reading differently through extensive tests and iterations of code.

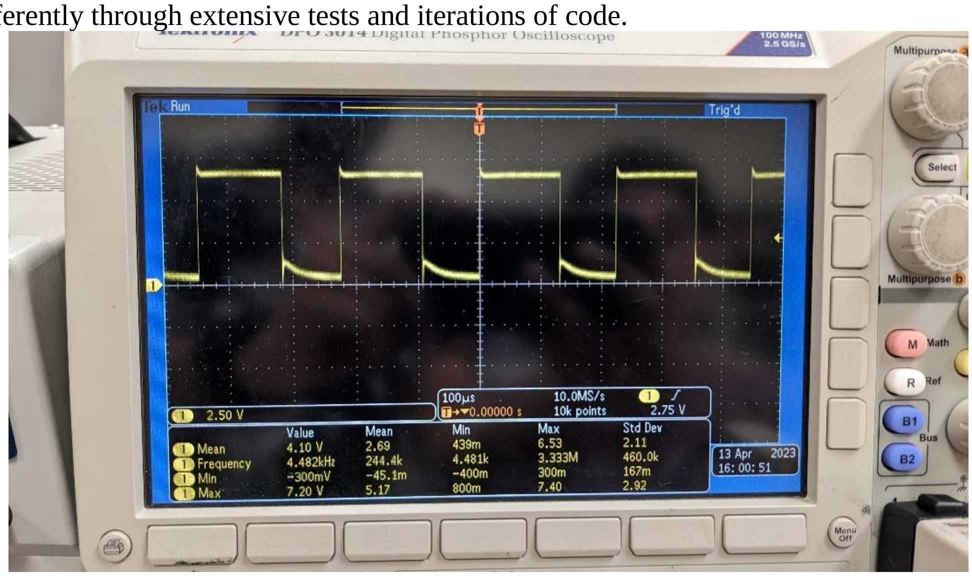

Figure 20: Testing of the MOSFET gate driver

The testing stage first involved writing pseudocode for each region and how the Teensy and MOSFET would react to different wind speeds, which were later translated into individual functions called to the main loop of the code. These functions were individually tested using the Teensy, a power supply, and an oscilloscope. As the voltage of the power supply was increased, the test code would detect different regions of operation and call the appropriate function to determine the optimal PWM value (that corresponds to optimal power), reflected on the oscilloscope, at that wind speed. This is how we determined that our PI control also worked to react quickly enough to any changes between operation regions.

5. Commissioning Checklist

In order to facilitate the ease of installation of our turbine during wind tunnel testing as well as maximize safety, our team has developed the following commissioning checklist. This checklist should be followed during the installation process to ensure proper procedures are followed.

#	**Step Details**
1	Secure the linear actuator, generator, and pitch actuation system by tightening the corresponding fasteners
2	Insert the blade mounts into the hub and secure each blade into its blade mount
3	Route wires from the turbine nacelle through the turbine tower
4	Secure the nacelle cover onto the top of the turbine
5	Attach the nacelle onto the tower clamp by tightening the corresponding screws
6	Loosely attach the tower clamp onto the turbine tower by using a press-fit
7	Route all wires through the foundation and out the appropriate hole to keep connectors dry before installation
8	Install the foundation into the sand and water tank
9	Attach the adapter stub onto the top of the foundation tubing
10	After moving the foundation under the tunnel, attach the turbine base onto the top of the adapter flange and tighten the wingnuts
11	Adjust the tower clamp as needed to the desired yaw and tighten the tower clamp

References

[1] J. F. Manwell, J. G. McGowan, and A. L. Rogers, *Wind Energy explained*. Chichester: John Wiley, 2002.

[2] R. G. Budynas, J. K. Nisbett, K. Tangchaichit, K. Tangchaichit, and J. E. Shigley, *Shigley's Mechanical Engineering Design*. New York, NY: McGraw-Hill, 2021.

[3] "Wing Bending Calculations." Available: http://web.mit.edu/16.unified/www/archives%202007-2008/spring%20temps/psets/systems/beambend.pdf

[4] A. Kalmikov, "Wind Power Fundamentals." Available: http://web.mit.edu/wepa/WindPowerFundamentals.A.Kalmikov.2017.pdf

[5] "Wind Energy Factsheet," *Center for Sustainable Systems*, 2021. https://css.umich.edu/publications/factsheets/energy/wind-energy-factsheet

[6] HEXION, "Epikote™ resin MGS™ RIMR 135 and epikure™ curing agent," Aug-2006. [Online]. Available: https://www.metyx.com/wp-content/uploads/PDF_Files/Hexion/TDS/TDS%20RIMH%20137.pdf. [Accessed: 05-May-2023].

[7] STPS20SM60 Power Schottky Rectifier - STMicroelectronics. (2011, October). Retrieved December 8, 2022, Available: https://www.st.com/content/ccc/resource/technical/document/datasheet/6b/54/c3/dc/15/fc/4b/d5/DM0003 4849.pdf/files/DM00034849.pdf/jcr:content/translations/en.DM00034849.pdf

[8] "RP17-DataSheet-US.pdf | ElectroCraft," *www.electrocraft.com*. https://www.electrocraft.com/pdf.php?pdf=files/downloads/Datasheets/bldc/RP17-DataSheet-US.pdf (accessed May 05, 2023).

[9] M. Molitch-Hou, "FEA analysis and predicting the performance of 3D printing," *Engineering.com*, 07-Nov-2016. [Online]. Available: https://www.engineering.com/story/fea-analysis-and-predicting-the-performance-of-3d-printing. [Accessed: 04-May-2023].

[10] "How does part orientation affect a 3D print? practical design tips for additive manufacturing," *Hubs*. [Online]. Available: https://www.hubs.com/knowledge-base/how-does-part-orientation-affect-3d-print/. [Accessed: 04-May-2023].

[11] Xie, H., Guo, E. (2019, July). How the Switching Frequency Affects the Performance of a Buck Converter. Retrieved December 8, 2022, from https://www.ti.com/lit/an/slvaed3/slvaed3.pdf

[12] Teensy® 4.1 Development Board. PJRC. (n.d.). Retrieved December 8, 2022, from https://www.pjrc.com/store/teensy41.html

[13] U.S Department of Energy. (2022, August 31). Collegiate Wind Competition 2023 Rules and requirements. Retrieved December 8, 2022, from https://www.energy.gov/sites/default/files/2022-09/cwc-2023-rules-requirements.pdf

[14] Polytek, "TINSIL® 80-series silicone rubbers technical bulletin - polytek," 19-Jan-2021. [Online]. Available: https://polytek.com/content/pdf/technicalbulletin/Polytek_TB_80Series_5-5-2021.pdf. [Accessed: 05-May-2023].